

31 simulations illustrate the considerable extent of synoptic-to-interannual variability in
32 the physics and biology of shelf seas. In discussion, the present limitations of S2P3-R
33 are emphasised, and future developments are outlined.

34

35 **1. Introduction**

36 In a global context, the shelf seas are disproportionately productive due to the
37 continuous supply of nutrients (Holt et al., 2009a, and references therein). A variety
38 of models have been developed to explore the processes that shape and maintain
39 productivity. Operational biogeochemistry and ecosystem models typically represent
40 the system with relatively high complexity and resolution, e.g., the 7 km Atlantic
41 Margin Model NEMO-ERSEM (AMM7-NE) system (Edwards et al., 2012) – see also
42 <http://www.metoffice.gov.uk/research/news/marine-predictions>. Such models may
43 perform well alongside observations, but simulations rely on high performance
44 computing resources such that extensive experimental work is consequently not
45 practical.

46 In contrast to complex models, the Shelf Sea Physics and Primary Production (S2P3)
47 model (Simpson and Sharples, 2012) exploits the dominance of vertical processes
48 over horizontal processes in shelf seas. S2P3 explicitly represents vertical heat fluxes,
49 vertical mixing of momentum, and vertical mixing of heat and tracers (nitrate and chl-
50 a concentrations). Central to the model physics is a turbulence closure scheme,
51 determining the light environment and nutrient fluxes that drive a simple primary
52 production (nutrient-phytoplankton, or NP) model. Phytoplankton growth responds to
53 changes in stratification and mixing. In this way, S2P3 can efficiently simulate the
54 seasonal cycle of stratification and primary production at a selected location,
55 characterized by a local depth and tidal current amplitude. In particular, S2P3 has
56 been used (e.g., Sharples, 2008) to simulate idealized seasonal tidal mixing fronts
57 (TMFs), analogous to the observed discontinuities between mixed and seasonally
58 stratified water in mid-latitude shelf seas (Simpson and Hunter, 1974). While
59 controlled to first order by vertical processes, the transition from mixed to stratified
60 water across a TMF typically occurs on a horizontal scale of ~10-20 km (e.g., Moore
61 et al., 2003), so for clear resolution of associated physical and biogeochemical
62 structures, TMFs are ideally simulated at high horizontal resolution (1-2 km).

63 S2P3 was introduced as PHYTO-1D and originally described in Sharples (1999). An
64 updated version of PHYTO-1D was described in Sharples (2008). The model is
65 designed for use as an investigative (and educational) tool (see zipped material at
66 <http://pcwww.liv.ac.uk/~jons/model.htm>). S2P3 has been used as a research tool to
67 establish the varying influence of winds and air-sea heat fluxes on inter-annual
68 variability in the timing of stratification and the spring bloom in the northwestern
69 North Sea (Sharples et al., 2006), and to quantify the impact of spring-neap tidal
70 cycles on biological productivity at TMFs (Sharples, 2008). In educational contexts,
71 S2P3 and forerunner models have been used for around 10 years in Year 3
72 undergraduate and masters level postgraduate teaching at the Universities of
73 Southampton and Liverpool, in the UK.

74 In spite of potential for widespread application, S2P3 has not been extensively used
75 and tested across real transects or in limited regions, where the model can be
76 appropriately used for investigating time-evolving stratification and biological
77 productivity. Introduced here, S2P3-R is a framework for using S2P3 to efficiently
78 model physical and biological structures in shelf seas, for selected years during the
79 reanalysis era (Kalnay et al., 1996). The development of S2P3-R has facilitated the
80 simulation of vertical processes and their horizontal variability in real-time, for quick
81 investigation of ongoing changes and detailed fieldwork planning.

82 In the remainder of the paper, we first outline the S2P3-R framework. We start with a
83 brief description of the physical and biological components of S2P3, followed by
84 details of the modified source code, model performance and diagnostic options. This
85 is in turn followed by details on model setup in different domains (horizontal meshes
86 and tidal forcing), and the specification of meteorological forcing. We then evaluate
87 model simulations for four different regions, undertaken and diagnosed using the new
88 framework. In discussion, some important caveats are emphasised, and we outline the
89 prospects for development of the S2P3-R framework.

90

91 **2. The S2P3-R framework**

92 *2.1 S2P3*

93 Here, we provide a brief description of the physical and biological components of
 94 S2P3, emphasizing key equations. For a more detailed model description, the reader is
 95 referred to Sharples (1999) and Sharples (2008).

96

97 *2.1.1 Physical model*

98 Central to the physics of S2P3 is a turbulence closure scheme, for which the
 99 prognostic variable is turbulent kinetic energy (TKE), formally defined as $q^2/2$, where
 100 q is the turbulent intensity, or velocity scale (m s^{-1}). For a tidal current with x- and y-
 101 components u and v , the tendency of TKE is expressed as

102

$$103 \quad \frac{\partial}{\partial t} \left(\frac{q^2}{2} \right) = \frac{\partial}{\partial z} \left(K_q \frac{\partial}{\partial z} \left(\frac{q^2}{2} \right) \right) + N_z \left[\left(\frac{\partial u}{\partial z} \right)^2 + \left(\frac{\partial v}{\partial z} \right)^2 \right] + K_z \left(\frac{g}{\rho} \frac{\partial \rho}{\partial z} \right) - \frac{q^3}{B_1 l} \quad (1)$$

104

105 where ρ is density, quadratic in temperature T ($\rho = 1028.11 - 6.24956 \times 10^{-2}T -$
 106 $5.29468 \times 10^{-3}T^2$, assuming a constant salinity of 35.00), B_1 is a constant of the
 107 closure scheme, K_q is the vertical eddy diffusivity for TKE, K_z is the vertical eddy
 108 diffusivity for other scalar properties, N_z is vertical eddy viscosity, and l is an eddy
 109 length-scale [$l = \kappa z(1 - z/h)^{0.5}$, at depth z , given total depth h and von Karmen's
 110 constant $\kappa = 0.41$]. Forward time stepping is explicit throughout, with time-steps, Δt ,
 111 constrained by the diffusive stability criterion, $\Delta t < \Delta z^2/2N_z$, given depth intervals, Δz .

112

113 Tides and winds force the TKE profile for given boundary conditions:

114

$$115 \quad q_{z=h}^2 = B_1^{2/3} \frac{\tau_s}{\rho_{z=h}} ; \quad q_{z=0}^2 = B_1^{2/3} \frac{\tau_b}{\rho_{z=0}} \quad (2a,b)$$

116

117 where τ_s is the surface ($z = h$) stress due to the wind, and τ_b is the near-bottom ($z = 0$)
 118 stress due to tidal currents. The x- and y-components of wind stress are obtained as

119

120
$$\tau_{sx} = -c_d \rho_a u_w \sqrt{(u_w^2 + v_w^2)}; \quad \tau_{sy} = -c_d \rho_a v_w \sqrt{(u_w^2 + v_w^2)} \quad (3a,b)$$

121

122 given a drag coefficient c_d [$c_d = (0.75 + 0.067w) \times 10^{-3}$, for wind speed w], air density
 123 ρ_a ($= 1.3 \text{ kg m}^{-3}$), and u_w and v_w , the x- and y-components of wind. The x- and y-
 124 components of near-bottom stress are obtained as

125

126
$$\tau_{bx} = -k_b \rho_0 u_1 \sqrt{(u_1^2 + v_1^2)}; \quad \tau_{by} = -k_b \rho_0 v_1 \sqrt{(u_1^2 + v_1^2)} \quad (4a,b)$$

127

128 given a drag coefficient k_b ($= 0.003$), representative density for seawater ρ_0 ($= 1025$
 129 kg m^{-3}), and u_1 and v_1 , the x- and y-components of the current 1m above the seabed.
 130 See Sharples (1999) for further details on the subsequent calculation of K_z , K_q and N_z .

131 In addition to mixing, the water column is locally heated and cooled. The tendency of
 132 temperature (T) is obtained at each depth level as

133

134
$$\frac{\partial T}{\partial t} = \frac{\partial}{\partial z} \left(K_z \frac{\partial T}{\partial z} \right) + Q_h(z) \quad (5)$$

135

136 where z is height above the seabed and $Q_h(z)$ is the net heating at depth z .

137 Heat fluxes are formulated as follows. We first define a surface net heat flux (Q_{net}) as
 138 the sum of incoming shortwave radiation (Q_{SW}), long-wave back radiation (Q_{LW}), and
 139 latent and sensible heat exchange with the atmosphere (Q_{sens} and Q_{lat}):

140

141
$$Q_{net} = Q_{SW} - (Q_{LW} + Q_{sens} + Q_{lat}) \quad (6)$$

142

143 Incoming shortwave radiation, irradiance in the presence of clouds, is calculated as

144

145
$$Q_{SW} = (1.0 - 0.004C - 0.000038C^2) Q_{SW,c-s} \quad (7)$$

146

147 where C is cloud fraction, and clear sky irradiance, $Q_{SW,c-s}$, is obtained as

148

$$149 \quad Q_{SW,c-s} = S(1 - \alpha)f(\theta, t)(1 - \kappa_{SW}) \quad (8)$$

150

151 where S is the solar constant ($= 1368 \text{ Wm}^{-2}$), α is an atmospheric albedo ($= 0.24$),
152 $f(\theta, t)$ is a function representing the daily and seasonal variation in day length at
153 latitude θ , and κ_{SW} is a short-wave absorption coefficient ($= 0.06$). Long-wave
154 radiation is calculated as

155

$$156 \quad Q_{LW} = \varepsilon_{LW}(1.0 - 0.6 \times 10^{-4} C^2)(0.39 - 0.05q^{0.5})\sigma T^4 \quad (9)$$

157

158 where ε_{LW} is long-wave emissivity ($= 0.985$), q is vapour pressure ($q = Rq_s$, given
159 saturated vapour pressure $q_s(T)$ and relative humidity R), and σ is the Stefan-
160 Boltzmann constant ($\sigma = 5.67 \times 10^{-8} \text{ W m}^{-2} \text{ K}^{-4}$). Sensible heat flux is calculated using
161 the bulk formula:

162

$$163 \quad Q_{sens} = \rho_a c_p C_h U (T_s - T_a) \quad (10)$$

164

165 where c_p is the specific heat capacity of air ($c_p = 1004 \text{ J kg}^{-1} \text{ K}^{-1}$), C_h is a transfer
166 coefficient ($C_h = 1.45 \times 10^{-3}$), U is surface wind speed, T_s is the sea surface
167 temperature, and T_a is surface air temperature. Latent heat flux is calculated using the
168 bulk formula:

169

$$170 \quad Q_{lat} = \rho_a L_v C_e U (q_s - q) \quad (11)$$

171

172 where L_v is the specific heat capacity of air ($L_v = 2.5 \times 10^6 - 2.3 \times 10^3 T_s$), and C_e is a
173 transfer coefficient ($C_e = 1.5 \times 10^{-3}$).

174 The surface net heat flux is partitioned down the water column as follows. The red
 175 end of the spectrum, 55% of shortwave radiation, is assumed to be absorbed at the top
 176 depth level, hence the surface heating, $Q_{h,0} = 0.55Q_{SW} - (Q_{LW} + Q_{sens} + Q_{lat})$. The
 177 remaining 45% of insolation is available for heating at lower levels, distributed
 178 exponentially throughout the water column as a heating rate $Q_h(z)$, according to

179

$$180 \quad \frac{\partial Q_h}{\partial z} = -Q_h(z)(\lambda_0 + \varepsilon X_T(z)) \quad (12)$$

181

182 where λ_0 is an attenuation coefficient ($\lambda_0 = 0.1 \text{ m}^{-1}$) and ε is a pigment absorption
 183 cross-section ($\varepsilon = 0.012 \text{ m}^2 (\text{mg chl})^{-1}$), accounting for shading due to $X_T(z)$, the local
 184 chlorophyll-a (chl-a) concentration (mg chl m^{-3}), taking $X_T(z) = q^{chl} P_C$, for cell chl-
 185 a:carbon ratio, q^{chl} ($0.03 \text{ mg chl (mg C)}^{-1}$), and carbon concentration, P_C (see below).

186

187 *2.1.2 Biological model*

188 Phytoplankton is modelled in terms of an equivalent carbon concentration (P_C , units
 189 mg C m^{-3}) and internal cellular nitrogen (P_N). In each grid cell, P_C tendency is due to
 190 the net effect of vertical mixing, growth and grazing, according to

191

$$192 \quad \frac{\partial P_C}{\partial t} = \frac{\partial}{\partial z} \left(K_z \frac{\partial P_C}{\partial z} \right) + \mu P_C - G P_C \quad (13)$$

193

194 given a grazing impact rate G , and a growth rate, μ , that is a function of
 195 photosynthetically-active radiation:

196

$$197 \quad \mu = \mu_m \left(1 - e^{-(\alpha I_{PAR} \theta / \mu_m)} \right) - r^B \quad (14)$$

198

199 where α is the maximum quantum yield, I_{PAR} is the light availability, θ is the chl-
 200 a:carbon ratio, r^B is the respiration rate, and the maximum growth rate, μ_m , is given by

201

202
$$\mu_m = 1.16 \times 10^{-5} \left(\frac{Q - Q_{sub}}{Q_m - Q_{sub}} \right) 0.59 e^{0.0633T} \quad (15)$$

203

204 where $Q = P_N/P_C$ is the cell nitrogen quota, Q_{sub} is the subsistence nutrient:carbon
 205 quota, and Q_m is the maximum cell quota. The tendency for phytoplankton nitrogen
 206 (P_N) is similarly described as

207

208
$$\frac{\partial P_N}{\partial t} = \frac{\partial}{\partial z} \left(K_z \frac{\partial P_N}{\partial z} \right) + u P_C - G P_N \quad (16)$$

209

210 where the uptake rate u is obtained as a Michaelis-Menton function of the dissolved
 211 inorganic nitrogen concentration (DIN):

212

213
$$u = \left[u_m \left(1 - \frac{Q}{Q_m} \right) \frac{DIN}{(k_u + DIN)} \right] + \begin{cases} \mu Q, & \mu < 0 \\ 0, & \mu \geq 0 \end{cases} \quad (17)$$

214

215 given k_u , a half saturation coefficient for nutrient uptake, and u_m , a maximum nutrient
 216 uptake rate. The uptake of nitrogen leads to a tendency in dissolved inorganic nitrogen
 217 (DIN):

218

219
$$\frac{\partial DIN}{\partial t} = \frac{\partial}{\partial z} \left(K_z \frac{\partial DIN}{\partial z} \right) - \mu P_C + e G P_N \quad (18)$$

220

221 where e is the fraction of grazed phytoplankton cellular nitrogen recycled
 222 immediately back into the dissolved nitrogen pool.

223

224 Water column nitrogen is constantly restored towards an initial winter concentration,
 225 DIN_0 (mmol m^{-3}), by a flux of inorganic nitrogen from the seabed:

226

227
$$\frac{\partial DIN_1}{\partial t} = \frac{f_{DIN}}{\Delta z} \left(1 - \frac{DIN_1}{DIN_0} \right) \quad (19)$$

228

229 where DIN_1 is the dissolved nitrogen in the bottom depth cell of the model grid, Δz
230 (m) is the thickness of the model grid cell, and f_{DIN} ($\text{mmol m}^{-2} \text{s}^{-1}$) is the maximum
231 flux of dissolved nitrogen from the seabed into the bottom depth cell.

232

233 The values of biological parameters (G , μ_m , θ , r^B , Q_{sub} , α , u_m , Q_m , k_u , e , DIN_0 , f_{DIN}) are
234 as listed in Table I of Sharples (2008).

235

236 *2.2 Modified S2P3 source code, performance and diagnostics*

237 For the S2P3-R framework, we modified the Fortran 90 source code of S2P3 v7.0,
238 which includes additional commands and subroutines to facilitate the Winteracter
239 Fortran GUI toolset (Interactive Software Services Ltd., www.winteracter.com), the
240 model being supplied with a text book (Simpson and Sharples, 2012) as an executable
241 application that runs under the Windows operating system. This source code was
242 modified for compilation and execution in a Unix environment by removing GUI-
243 related lines of code. These changes are solely to facilitate compilation and execution
244 in Unix environments, and S2P3 is thus far unchanged as a scientific tool.

245 Within the new framework, S2P3 can be used to generate geographically specific
246 maps, sections and time series, with varying run-time implications on a single
247 processor. Maps typically comprise 5000-20000 grid-points, while sections comprise
248 10-100 grid-points. For a given year (see below), maps can take over a day to
249 generate (depending on the extent of shallower water, where shorter time-steps are
250 necessary), while sections typically take a few minutes, and annual time series at a
251 single location typically take a few seconds.

252 Default mapped variables are the mid-summer surface-bottom temperature difference,
253 annual-mean surface heat flux, and annual net production. Other quantities, such as
254 the mid-summer sub-surface chl-a maximum (SCM) and SCM depth, can also be
255 mapped. The option for simulating sections is motivated by opportunities for direct
256 comparison with measurements obtained through surveys and cruises. In selecting to
257 simulate section data, constant depth intervals are specified for plotting on a regular
258 distance-depth mesh without the need for interpolation. The option for time series at
259 single locations is motivated by the availability of time series at repeat Conductivity
260 Temperature Depth (CTD) stations and moorings. Finally, we save daily horizontal

261 distributions of physical and biological variables for selected periods, to generate
262 animations that yield a range of insights not so easily appreciated with individual
263 maps or sections.

264 FORTRAN programmes are used to post-process model data for plotting, and
265 MATLAB scripts are used to plot model variables (as used to prepare the figures and
266 animations presented here). Example MATLAB plotting scripts are provided together
267 with the source code and other ancillary programmes and data files in s2p3-reg.zip
268 (see “Code availability”).

269

270 *2.3 Regional configurations*

271 Three domains have been developed and tested here, for reasons that are outlined in
272 turn. Figure 1 shows the bathymetry, while Table 1 specifies the boundaries,
273 resolution, tidal forcing and initial temperature field, for each domain. In an initial
274 stage of development, S2P3-R was developed for the northwest European shelf
275 domain. Development of the two other domains has been motivated by the extent to
276 which the different climatological and tidal forcing can be accommodated (in the shelf
277 seas around China) and by ongoing fieldwork (annual surveys south of Cornwall) in a
278 smaller region where the tidal mixing front is particularly sharp.

279 Bathymetry is typically in the range 50-100 m across most of the northwest European
280 shelf (Fig. 1a). However, some important details are emphasised for the other two
281 domains: a shallower inshore zone (depths < 30 m) in the Western English Channel
282 (Fig. 1b); a secondary shelf break (descending 50-100 m) in the East China Sea (Fig.
283 1c). At very high resolution, some artefacts of bathymetric surveying are apparent as
284 linear features in the bathymetry south of Cornwall (Fig. 1b).

285 For the northwest European shelf, bathymetry and current amplitudes for the leading
286 three tidal constituents (M2, S2, N2 - see Fig. S1 in Supplementary Material) were
287 obtained from the POLCOMS model (e.g., Holt et al., 2009b). For the Western
288 English Channel, bathymetry is extracted from the ETOPO1 global relief model
289 (Amante and Eakins, 2009) and tidal current amplitudes are interpolated from the
290 POLCOMS dataset. For the East China and Yellow Seas, current amplitudes for the
291 leading 13 tidal constituents were generated using OTPS (OSU Tidal Prediction
292 Software), based on the inverse method developed by Egbert et al. (1994) and Egbert

293 and Erofeeva (2002), and bathymetry is selected within the OTPS system. Opting to
294 use the leading five constituents for this region, S2P3 was adapted to include the two
295 diurnal constituents, O1 and K1, in addition to the semi-diurnal constituents S2, M2
296 and N2 (see Fig. S2).

297 One further distinction in regional setup concerns initial temperatures. At 1 January of
298 each year, the water column across the European shelf seas is presumed mixed
299 everywhere. In the default model, initial temperature is 10.1°C at all depths,
300 appropriate for the Celtic Sea. This initial temperature is also appropriate for the
301 Western English Channel, although we specify simulated 31 December temperatures
302 (constant through the fully mixed water column) for subsequent 1 January dates in the
303 case of simulations at the Western Channel Observatory (see Section 3.2). Elsewhere,
304 alternative values for initial temperature are appropriate, consistent with local climate.
305 Consider as an example the northeast sub-region of our northwest European shelf
306 domain. Sensitivity tests illustrate the importance of specifying an appropriate initial
307 temperature – see Fig. S3. If the initial temperature in this region is too high (Fig.
308 S3a), the net heat fluxes fall below -10 Wm^{-2} across much of the domain, especially to
309 the north (i.e., annual net cooling from a “warm start”), while if the temperature is too
310 low (Fig. S3b), heat fluxes exceed 10 Wm^{-2} at most locations (i.e., annual net
311 warming from a “cold start”). Only if the initial temperature is accurate to within
312 around 1°C do we avoid strong annual net cooling or heating (Fig. S3c). For the
313 China Seas, we specify a higher initial temperature of 15.1°C and simulate two
314 consecutive years, accounting for weak wintertime stratification in this region. We
315 analyse only the second year, for which more realistic initial conditions are thus
316 established across the wider domain (on 1 January of the second year).

317

318 *2.4 Meteorological forcing*

319 In addition to tidal mixing, S2P3 is forced with surface heat fluxes and wind stirring.
320 Heat is gained by shortwave radiation and lost via long-wave back-radiation, sensible
321 and latent heat fluxes - see Eqn. (6). Shortwave radiation varies with latitude and time
322 of year, and decreases with fractional cloud cover - see Eqns. (7) and (8). Long-wave
323 radiation varies with sea surface temperature and cloud cover – see Eqn. (9). Sensible

324 and latent heat losses vary with air temperature, wind speed and relative humidity
325 according to bulk formulae – see Eqns. (10) and (11).

326 Daily values for the four necessary meteorological variables are provided in a single
327 ASCII file. Sharples (2008) uses climatological meteorological data for the Celtic
328 Sea, while Sharples et al. (2006) use meteorological data for 1974-2003 from weather
329 stations in the vicinity of a study site in the northwestern North Sea. Here, we use
330 NCEP Reanalysis data provided by the NOAA/OAR/ESRL PSD, Boulder, Colorado,
331 USA, from their website at <http://www.esrl.noaa.gov/psd/>. These data are routinely
332 updated to within a day or so of the present time, and span the period from 1948. The
333 data is provided on a 2.5° global mesh, so each domain is forced everywhere with
334 meteorological data from a single 2.5° grid square, central to that region. Coordinates
335 of selected grid squares are listed in Table 1.

336 Figure 2 illustrates time series of meteorological variables for the three domains. In
337 initial testing, for the northwest European shelf, we use the “default” Celtic Sea
338 climatology (Sharples, 2008). For the other two domains, data for 2013 are shown for
339 example. Note the extent of high-frequency synoptic variability in these cases, in
340 particular for relative humidity, cloud fraction and wind speed. Also note that the UK
341 spring of 2013 was exceptionally cold, hence air temperatures for the Western English
342 Channel sub-domain considerably below the Celtic Sea climatological average. Also
343 note considerable contrast between the maritime and continental climates, for the
344 European shelf and China Seas respectively.

345

346 **3. Model evaluation in the new framework**

347 *3.1 Northwest European shelf*

348 Figure 3 shows a summary of fields obtained for a simulation using the northwest
349 European shelf domain. Fig. 3a shows the annual-mean Hunter-Simpson parameter,
350 $\log_{10}(h/u^3)$, where h is the local depth and u is the amplitude of the local tidal current.
351 Previous studies (starting with Simpson and Hunter, 1974) have established a
352 threshold value of around 2.7, below (above) which the water column is well mixed
353 (stratified). $\log_{10}(h/u^3)$ is generally below 2.7 throughout the southern North Sea, and
354 across much of the eastern English Channel and the Irish Sea. These regions are
355 indeed well mixed throughout summer, as evident in near-zero surface-bottom

356 temperature differences for mid-July, shown in Fig. 3b. Elsewhere, stratification is
357 established, and the model hence simulates a set of fronts between mixed and
358 stratified water that are clearly observed in satellite data (see Fig. 8.1 in Simpson and
359 Sharples, 2012 - also indicated in Fig. 3a): the Islay front between Northern Ireland
360 and Scotland (A); the Western Irish Sea front enclosing a seasonally-stratified region
361 of the Irish Sea (B); part of the Cardigan Bay front (C); the St George's Channel front
362 between Wales and Ireland (D); the Ushant and Western English Channel front
363 between southwest England and Brittany, France (E). The model also simulates a
364 front observed between the seasonally-stratified northern North Sea and the
365 permanently mixed southern North Sea, including the Flamborough frontal system
366 (Hill et al., 1993, and references therein), also indicated (F) in Fig. 3a.

367 A limitation of the simulation presented in Fig. 3 is the use of default climatological
368 meteorological forcing, originally set up for simulating tidal mixing fronts in the
369 Celtic Sea. This has important consequences for local heat balances, evaluated here
370 with the annual-mean surface net heat flux, shown in Fig. 3c. In the central Celtic Sea
371 (south of Ireland), the net heat flux is slightly positive, in the range $0-5 \text{ Wm}^{-2}$.
372 Elsewhere, one might expect that a warmer (cooler) sea surface will lead to stronger
373 net heat loss (gain), via sensible and latent heat fluxes. However, the imbalance
374 reaches a maximum of 10 Wm^{-2} in the warm southwest English Channel (net heating)
375 and a minimum of -10 Wm^{-2} in the cool northern North Sea (net cooling). This is
376 consistent with insolation levels at these latitudes that are respectively higher and
377 lower than that for the Celtic Sea. Such imbalances are also a consequence of
378 specifying the same initial temperature everywhere (see section 2.2), such that the
379 northern North Sea is initially too warm (so must lose heat over the seasonal cycle),
380 and the southwest English Channel is initially too cool (so must gain heat). Net heat
381 fluxes are also notably positive in some regions that are well mixed all year round, in
382 particular the Irish Sea and parts of the English Channel. This is consistent with
383 enhanced heat storage due to mixing throughout the water column of heat gained in
384 summer (Simpson and Bowers, 1984).

385 We have also experimented, on the northwest European shelf domain, with spatially
386 discriminate initial temperatures and meteorological forcing (not shown here), the
387 latter respecting variation of NCEP reanalysis data (per 2.5° grid square) across the
388 domain. While this approach has the potential to restrict net heat fluxes closer to zero

389 at all locations, coarse-resolution data must be carefully interpolated to the relatively
390 fine 12-km mesh of S2P3-R in order to avoid unrealistic horizontal variations in
391 forcing and simulated fields.

392 Depending on temperature and the co-availability of photosynthetically active
393 radiation (PAR) and nutrients, the model simulates primary production. Annual net
394 carbon production per unit area is shown in Fig. 3d and simulated surface chl-a is
395 compared to satellite observations in Fig S4 and S5. The model broadly reproduces
396 the temporal and spatial variability in primary production and chl-a observed across
397 the shelf, although considerable improvements can be achieved through tuning of key
398 model parameters (work in progress).

399 Surface production rates (Fig 3d) and chl-a concentrations (Fig. S4) are especially
400 high in shallow coastal water that remains well mixed for most/all of the year, where
401 nutrients are consequently continuously re-supplied from the seabed, and PAR levels
402 are sufficient at all depths to maintain photosynthesis. We have limited confidence in
403 the simulated primary production and chl-a close to the coasts, for two specific
404 reasons. We do not account for the strong influence near many coasts of freshwater
405 (runoff), which has an important stratifying influence on the water column. We also
406 neglect the higher turbidity caused by non-algal particles that can reduce PAR below
407 a level necessary to sustain photosynthesis, e.g., where sediment loads are relatively
408 high in shallow regions of vigorous mixing, such as the southern North Sea.
409 Recognizing this model limitation, we choose not to plot model output in water
410 shallower than 30 m in Figs. 3 and S4.

411 Moving towards stratified regions, annual-mean carbon production rates generally
412 decline, although remain above $55 \text{ g C m}^{-2} \text{ year}^{-1}$ at most locations due to the
413 combined result of the major spring and minor autumn blooms (see below). This
414 decline is complemented by elevated productivity throughout summer at the
415 thermocline, associated with the development and persistence of the sub-surface chl-a
416 maximum (SCM). Primary production rates during the spring bloom (not shown)
417 reach $40 \text{ g C m}^{-2} \text{ mon}^{-1}$ or $1333 \text{ mg C m}^{-2} \text{ d}^{-1}$, in line with observed magnitudes in the
418 order of $1000 \text{ mg C m}^{-3} \text{ d}^{-1}$ (Rees et al., 1999). Summertime chl-a and primary
419 production are low in the surface mixed layer, consistent with observed values of <1
420 mg chl-a m^{-3} and $5\text{-}30 \text{ mg C m}^{-3} \text{ d}^{-1}$, respectively (Joint et al., 2000; Hickman et al.,
421 2009). Simulated surface chl-a concentrations are broadly consistent with satellite

422 observations, although values are typically double those observed (see Figs. S4 and
423 S5). The model does not reproduce the enhanced primary production and chl-a
424 observed in the surface at the Celtic Sea shelf break (e.g., compare Figs. S4 and S5,
425 for April and May). This is likely because it does not include specific physical
426 processes, such as the internal tide, that are important for vertical nutrient supply to
427 the surface in these regions (Sharples et al., 2007).

428 Following the spring bloom, surface productivity and surface chl-a concentrations
429 remain elevated (above background values) near three tidal mixing fronts in particular
430 – the Ushant and Western English Channel front, the Islay front, and the St George’s
431 Channel front – for June-September in the simulation (Fig. S4) and for May-July in
432 the observations (Fig. S5). Surface chl-a concentrations decline towards more
433 stratified waters, coincident with deepening of the SCM away from fronts and
434 associated zones of spring-neap frontal adjustment (Pingree et al., 1978; Weston et al.,
435 2005; Hickman et al., 2012). At the Ushant Front, predicted peak July primary
436 production of 80-100 mg C m⁻³ d⁻¹ is considerably smaller than in situ measurements
437 of 59-126 mg C m⁻³ h⁻¹ (implying daily production of around 1000 mg m⁻³ d⁻¹), for
438 surface waters at a frontal station in late July (Holligan et al., 1984). However, the
439 model estimates are intermediate between corresponding surface observations for
440 mixed and stratified waters (reported in Holligan et al., 1984), emphasizing the very
441 localized character of frontal productivity, which is not easily captured with our
442 relatively coarse model resolution (here around 12 km) and in the absence of
443 horizontal processes that may lead to convergence of material at the front.

444 In the southern Irish Sea and south of the Islay front, simulated surface chl-a
445 concentrations are notably very low, at around 0.1 mg chl-a m⁻³ (see Fig. S4). These
446 low values are found in regions where the tidal current amplitude is especially strong
447 (see Fig. S1) in water that is sufficiently deep (~100 m, see Fig. 1a) for PAR to fall
448 below a threshold value within the well-mixed water column (Fig. 3b). So in spite of
449 very high nutrient levels throughout the year (not shown), light is a severe limitation
450 on photosynthesis and hence productivity. This aspect of the simulation is inconsistent
451 with surface chl-a concentrations of around 1 mg chl-a m⁻³ observed in this region
452 (Fig. S5; Pemberton et al., 2004; Moore et al., 2006). A likely explanation is that the
453 model does not resolve photo-acclimation, the known ability of phytoplankton to
454 acclimate to ambient light conditions (e.g., Geider et al., 1997), and so does not

455 resolve the photo-physiological differences between stratified and mixed water
456 columns (Moore et al., 2006). Dissolved inorganic nitrate (DIN) concentrations in the
457 northwest European shelf region during winter and in the bottom mixed layer during
458 summer (not shown) are 5-6 mmol m⁻³, consistent with observed values around 6-9
459 mmol m⁻³ (Joint et al., 2001; Hickman et al., 2012).

460 To illustrate typical vertical structure across a mid-summer tidal mixing front, Figure
461 4 shows observations and corresponding simulations for day 215 (3 August) of 2003,
462 along a section through the Celtic Sea front (Fig. 4a), located at around 52°N. The
463 temperature distribution (Fig. 4b,c) illustrates stratified water south of 52°N, with
464 mixed water to the north. DIN concentrations are high in mixed water and in the
465 lower layer of the stratified water, and depleted in the surface layer of the stratified
466 water (Fig. 4d,e). Chl-a concentrations reach a surface maximum at the front, with
467 elevated values extending southwards in the model - the SCM supported by a weak
468 diffusive DIN flux across the thermocline (Fig. 4f,g).

469 Comparing the simulation with the observations, the mixed water is about 1°C cooler
470 than observed, and DIN and chl-a concentrations are about 50% higher at most
471 depths. Regarding structural discrepancy between observed chl-a concentrations in
472 Fig. 4f and modeled chl-a concentrations in Fig. 4g, the northward-shifted surface
473 maximum in the model is coincident with a more northward location of the tidal
474 mixing front, which could be attributed to inadequacies in meteorological and/or tidal
475 forcing. The higher surface maximum of chl-a in the model may be in part due to
476 neglected horizontal processes, such as along-front transports by a baroclinic jet
477 supported by strong horizontal temperature gradients, and cross-frontal mixing
478 processes associated with jet instability. Higher chl-a concentrations in the model may
479 alternatively be attributed to the relatively simple description of phytoplankton
480 physiology, grazing and mobility (no sinking, as default).

481

482 3.2 *Western English Channel*

483 For 1 May to 7 October of 2013, selected daily model fields are saved and animated
484 (see Supplementary Material Part B, “Example Animation”, and accompanying
485 commentary text). A wide range of phenomena are evident in the animation, including
486 the earliest establishment of stratification during May, expressed as a surface-bottom

487 temperature difference, and the rapid uptake of surface DIN, which declines to near-
488 zero concentrations with the development of a spring bloom (high surface chl-a
489 levels) that peaks in early-mid June. We note that the exceptionally cold spring of
490 2013 substantially delayed the onset of stratification and the spring bloom (also
491 suggested by satellite data – not shown). The spring-neap cycle of stronger mixing (on
492 spring tides) and strengthened stratification (on neap tides) causes ~14-day “beating”
493 of chl-a concentration, between low values on spring tides and high values on neap
494 tides, most notably at the front between inshore mixed and offshore stratified waters
495 off southwest Cornwall throughout June and July.

496 To illustrate the interannual variability of summer stratification, Figure 5 shows
497 surface-bottom temperature differences on day 190 (8 or 9 July) of 2002-13. The
498 region is characterized by mixed water to the northwest associated with locally strong
499 tidal current amplitudes (see Fig. S1), and stratified water to the southwest (where
500 tides are weaker), with a secondary area of stratification centred around 4.5° W 50.1°
501 N (coincident with a local minimum in tidal current amplitude). The water column
502 remains mixed all year round in shallow water close to the coast, at most locations
503 and in most years. A complex arrangement of mixed and stratified water is simulated
504 in the northeast of the region, associated with highly variable bathymetry (see Fig.
505 1b). When a cold spring is followed by a warm summer (e.g., 2006, 2010, 2013),
506 stratification is particularly strong, with surface-bottom temperature differences
507 reaching almost 7°C in the southwest of the region.

508 To locally validate the simulation, we use observations at L4 (50° 15.00' N, 4° 13.02'
509 W) and E1 (50° 02.00' N, 4° 22.00' W), hydrographic stations that have been occupied
510 weekly and monthly, respectively, as part of the Western Channel Observatory
511 (<http://www.westernchannelobservatory.org.uk/data.php>). Here, seasonal cycles of
512 stratification and phytoplankton dynamics have been extensively studied (Smyth et al.
513 2010). In Fig. 5, we over-plot observed temperature differences for station
514 occupations within a few days (L4) or 1-2 weeks (E1) of day 190. Observed
515 differences are generally indistinguishable from the simulated differences.

516 For a more comprehensive validation, Figure 6 shows time series of surface-bottom
517 temperature differences observed and (daily) simulated at L4 and E1. The temperature
518 at the depth of the maximum chl-a concentration is also plotted at E1, confirming the
519 existence of an SCM within the seasonal thermocline. Starting on 1 January 2002, we

520 simulate one year at a time, specifying a mixed water column temperature on, e.g., 1
521 January 2003 with the corresponding temperature on 31 December 2002, etc. This
522 ensures continuity in temperatures between years, respecting a small degree of
523 interannual variability in wintertime temperature at L4 and E1. Weak stratification
524 (maximum $\sim 4^{\circ}\text{C}$) typically is established over ~ 5 months of each summer at L4,
525 while stronger stratification (up to $\sim 7^{\circ}\text{C}$) develops for longer (by 1-2 months) at E1.
526 Model-observation agreement is remarkably good, with close correspondence
527 between not just surface temperatures, but also bottom temperatures. The seasonally
528 varying stratification at both stations is generally reproduced to within 1°C , although
529 high-frequency extremes are under-sampled by weekly (monthly) occupations of L4
530 (E1), and there is more disagreement at L4. This is most likely because the water
531 column at L4 is strongly influenced by freshwater, with low surface salinity having a
532 substantial effect on stratification. The vertical salinity distribution also explains the
533 apparent temperature instability (negative surface-bottom temperature differences)
534 observed at L4 in winter - the water column is in fact statically stable throughout the
535 time series.

536 With some confidence in model performance, in Figure 7 we show temperature, DIN
537 and chl-a in sections through the developing tidal mixing front east of Lizard
538 peninsula, along 50.017°N , on days 100, 130, 160 and 190 of 2013. We select this
539 section as representative of CTD transects undertaken annually in late June/early July
540 by University of Southampton fieldwork students. On day 100 (early April), the water
541 column is well mixed almost everywhere, with very weak stratification in temperature
542 evident at 10 km along the section. DIN concentrations are high ($\sim 6 \text{ mmol m}^{-3}$)
543 throughout the water column for bottom depths exceeding a threshold value ($\sim 40 \text{ m}$),
544 below which PAR falls below a critical value within the water column. As bottom
545 depths become shallower (progressing inshore), DIN concentrations rapidly fall to
546 near zero, where PAR is sufficient at all depths to sustain plankton growth and
547 associated DIN uptake in the model. Inshore chl-a concentrations are accordingly high
548 ($12\text{-}13 \text{ mg chl-a m}^{-3}$), falling rapidly with distance to background values ($\sim 0.1 \text{ mg}$
549 chl-a m^{-3}) offshore.

550 By day 130 (early May), the water remains well mixed, although warmer by $1\text{-}2^{\circ}\text{C}$,
551 and high productivity has spread offshore, presumably due to intermittent weak
552 stratification during preceding days. By day 160, stratification is clearly established

553 beyond 4 km offshore. DIN concentrations are now reduced to near-zero in the upper
554 20 m of the stratified water, and high chl-a concentrations are evidence of the spring
555 bloom. By day 190, stratification has strengthened and DIN concentrations in the deep
556 layer of stratified water columns are further depleted through vertical mixing with the
557 upper photic zone, although surface chl-a concentrations have by this time
558 substantially declined in the upper layer. The boundary between mixed and stratified
559 waters on days 160 and 190 marks the position of the tidal mixing front. The model
560 has been further used to evaluate the extent of interannual variability around the time
561 of annual fieldwork, in the third week of June. Temperature sections on day 169 of
562 2002-13 (see Figure S6) reveal a wide range of offshore stratification and frontal
563 structure in recent years, with strongest stratification in 2010, weakest stratification in
564 2011, and a most clearly defined front in 2009.

565 As an example of the seasonal cycles in temperature, surface DIN and surface chl-a at
566 four locations across the front (spanning the distance range 3-7 km in Fig. S6), Figure
567 8 shows evolution of these variables through 2013. Stratification is very marginal and
568 intermittent at 5.033°W, with surface-bottom temperature differences occasionally
569 reaching 2°C. DIN concentrations fall close to zero over days 130-300 and chl-a
570 concentrations are high (in the range 6-8 mg chl-a m⁻³ throughout this period. Related
571 to the intermittent stratification are similar fluctuations in chl-a. This variability is in
572 part attributed to the near-fortnightly spring-neap tidal cycle, which leads to periodic
573 replenishment of nutrients, out of phase with more favourable PAR regimes.
574 Progressing offshore into deeper water, the seasonal cycle transforms towards
575 stronger stratification, a shorter period of surface DIN reduction, and a stronger peak
576 in surface chl-a around day 150 that corresponds to the spring bloom, followed by
577 substantially lower concentrations during the rest of summer.

578

579 *3.3 East China and Yellow Seas*

580 Figure 9 shows example fields for a simulation using the East China Sea and Yellow
581 Sea domain with 2013 forcing. Fig. 9a shows the annual-mean Hunter-Simpson
582 parameter, $\log_{10}(h/u^3)$, which falls below 2.7 in particularly shallow regions (see Fig.
583 1c) that are also characterized by high amplitude tidal currents (see Fig. S2).
584 $\log_{10}(h/u^3)$ conversely exceeds 5.0 in the isolated Bohai Sea, lying to the northwest of

585 the Yellow Sea. As for the northwest European shelf, regions with $\log_{10}(h/u^3) < 2.7$
586 remain well mixed throughout summer (Fig. 9b). Elsewhere, stratification is stronger
587 than for the northwest European shelf, with surface-bottom temperature differences
588 on day 190 of $\sim 10^\circ\text{C}$ across much of the stratified shelf. A major feature of Fig. 9b is
589 the front between mixed and stratified water in the East China Sea that is clearly
590 observed in satellite SST data (Hickox et al., 2000). The simulations also capture the
591 complex system of fronts observed in the Taiwan Strait (Zhu et al., 2013).

592 The specification of common meteorological variables across $\sim 20^\circ$ of latitude and
593 $\sim 15^\circ$ of longitude is a considerable approximation, and the annual-mean net surface
594 heat flux field is an important measure of resulting heat imbalances (Fig. 9c). We
595 regard these values as not too excessive, ranging from around 5 Wm^{-2} (heat gain) in
596 the far south to around -10 Wm^{-2} (excess heat loss) in the far north (Bohai Sea).
597 Annual-mean carbon production rates in the well-mixed shallow regions of the East
598 China Sea range from 300 to $450 \text{ g C m}^{-2} \text{ year}^{-1}$, falling to $\sim 100 \text{ g C m}^{-2} \text{ year}^{-1}$ in the
599 more extensive stratified region (Fig. 9d). These predictions are similar in magnitude
600 to estimates of primary production based on in situ observations (e.g., 145 g C m^{-2}
601 year^{-1} for “the entire shelf of the East China Sea”, Gong et al. 2003). Monthly-mean
602 surface chl-a distributions are broadly comparable to satellite observations, although
603 maximum model chl-a concentrations are generally double those observed, and the
604 spring bloom is ~ 1 month late, in May rather than April (e.g., for 2013, Figs. S7 and
605 S8). Discrepancies between the model and observations in this region may be
606 improved by accounting for higher turbidity in relatively shallow water and model
607 refinements related to photo-physiology.

608 To complete the three-dimensional picture, Figure 10 shows show temperature, DIN
609 and chl-a concentration in sections through the developing front of the central East
610 China Sea, along 32°N , on days 100, 130, 160 and 190 of 2013. Bottom depth
611 increases considerably with distance offshore. In water of depth $< 40 \text{ m}$, the water
612 column remains well-mixed throughout the year, while in deeper water, stratification
613 becomes established between days 100 and 130. In stratified water, DIN is already
614 depleted in the surface layer over days 100-130, and is gradually further depleted in
615 the lower layer over days 130-190 through progressive mixing into the photic zone. A
616 local surface maximum in chl-a concentration is evident at the frontal boundary (~ 250

617 km) on day 130, while a SCM is evident in stratified water on days 160 and 190. The
618 SCM is most clearly defined at ~25 m on day 190.

619

620 **4. Summary and discussion**

621 We have developed S2P3-R, a versatile framework for efficient modeling of physical
622 and biological phenomena and processes in shelf seas, adopting an existing 1-D
623 model, S2P3. Here, we complement ongoing development and use of the 1-D model
624 for specific research hypotheses (e.g., Bauer and Waniek, 2013) and in educational
625 settings, where idealized simulations (e.g., Sharples, 2008) are linked to realistic
626 situations such as fieldwork contexts - e.g., off Cornwall, away from the lateral
627 influences of runoff.

628 The realism of S2P3-R depends on the extent to which vertical processes dominate
629 horizontal processes. This is evident across some shelf sea regions, where we have the
630 high-quality observations necessary for a co-evaluation of these processes. One way
631 to formally quantify the dominance of surface net heat fluxes and tidal plus wind
632 mixing (the 1-D processes) is by calculating tendencies of the potential energy
633 anomaly (PEA, see Chapter 6 in Simpson and Sharples, 2012). PEA tendencies
634 calculated directly from observed changes of stratification at selected locations (e.g.,
635 weekly/monthly at Western Channel Observatory stations L4/E1) can be compared
636 with indirect estimates computed from time-integrated heat fluxes, winds and tidal
637 currents at the same locations. If local heat fluxes and tidal/wind mixing dominate the
638 annual cycle of stratification, directly calculated and indirectly estimated time series
639 of PEA tendency should be similar.

640 Where appropriate, the framework facilitates experiments to investigate the sensitivity
641 of measurable quantities (e.g., chl-a concentration) to a wide range of physical and
642 biological processes that can be adjusted with corresponding model parameters.
643 Where high quality observations are available (e.g., at E1 in the western English
644 Channel), S2P3-R thus provides a means for improving our fundamental
645 understanding of the system. With tuned parameters, S2P3-R furthermore provides
646 the means to carry out credible multi-year simulations of physical and biological
647 processes and property distributions at appropriately high temporal, vertical and
648 horizontal resolution.

649 At the seasonal timescale, the most striking surface features are tidal mixing fronts
650 (TMFs). Realistic representation of TMFs, demanding high horizontal resolution,
651 amounts to first-order evaluation of any simulation, e.g., the UK Met Office forecast
652 system (O’Dea et al., 2012), which has the same relatively coarse (12 km) resolution
653 as our northwest European shelf domain. The summer surface-bottom temperature
654 differences across the northwest European shelf and the associated TMFs in S2P3-R
655 (Fig. 3a) compare well with the 3-D model results (O’Dea et al., 2012, their Fig. 10).
656 Our simpler approach thus indicates the importance of 1-D processes in forming these
657 features, the locations of which are consistent with these more complex models.

658 It is natural to deploy S2P3 across multiple processors, with sub-domains computed
659 independently in parallel. This has been trialled for twelve $1^\circ \times 1^\circ$ sub-domains across
660 the southern Celtic Sea and western English Channel at a resolution of 1 km,
661 substantially expanding our Western English Channel domain with essentially no
662 extra computational expense. Figure 11 shows the July surface-bed temperature
663 difference across this region, illustrating how we are able to efficiently simulate
664 regional stratification at very high horizontal resolution.

665 We have evaluated the model in various ways with available observations,
666 specifically addressing spatial patterns, vertical structures, and seasonal-interannual
667 variability. Temperature distributions are reproduced with considerable success, as are
668 key aspects of the spatial and temporal variability in nutrient and chl-a concentrations.
669 In particular, we are able to accurately reproduce monthly observations of thermal
670 structure at station E1 in the western English Channel over 2002-13 (Fig. 6),
671 providing confidence in the use of S2P3-R in this region. We therefore consider there
672 is much potential for S2P3-R to investigate physical and physiological controls on
673 primary productivity at regional scales.

674 Elsewhere, differences between the model and observations are informative because,
675 for example, they identify regions in which processes other than those represented in
676 the model are important. In particular, we note several processes specific to coasts and
677 shelf breaks, of relevance to several physical aspects of the domains considered here:

- 678 • The coastal zone around Cornwall, typified by station L4, is strongly
679 influenced by riverine inputs that promote surface freshening and stratification

680 and alter light attenuation by non-algal particles and dissolved organic matter
681 (Groom et al., 2009; Smyth et al., 2010)

682 • The northern North Sea is strongly influenced by shelf edge exchange that
683 leads to the inflow of relatively warm and salty Atlantic Water (Huthnance et
684 al., 2009)

685 • The Yangtze River and two branches of the Kuro Shio - the Taiwan Current
686 and the Tsushima Warm Current - exert strong influences on stratification and
687 productivity in the East China Sea (e.g., Son et al., 2006).

688 Further development of S2P3-R will formally establish the (presently prototype)
689 option to prescribe spatially variable initial temperatures and meteorological
690 variables, interpolated appropriately to each model mesh. As an additional diagnostic,
691 the thermal wind balance may be used with the simulated density field to infer the
692 residual flows that are associated with TMFs (e.g., Hill et al., 2008), indicating the
693 potential importance of net advection along the fronts.

694 In summary, the S2P3-R framework (v1.0) provides the flexibility to undertake
695 research experiments in finely-resolved realistic domains where 1-D processes
696 dominate, to test hypotheses regarding the sensitivity of 1-D biogeochemical
697 processes to key model parameters, and/or to test the responses to variations of
698 physical forcing on timescales ranging from diurnal to interannual. Combining
699 flexibility with computational efficiency, the S2P3-R framework may further
700 contribute to capacity building in marine monitoring and management for
701 individuals/organisations without the resources to run or analyse complex models of
702 their territorial waters or exclusive economic zones.

703

704 **Code availability**

705 The S2P3-R (v1.0) framework, comprising source code along with example scripts
706 and output, is available online from:

707 `ftp://ftp.noc.soton.ac.uk/pub/rma/s2p3-reg.tar.gz`

708 Unzipped and uncompressed, the directory `/s2p3_reg_v1` contains several sub-
709 directories:

- 710 • /main contains the source code, `s2p3v7_reg_v1.f90`, which is compiled
711 “stand-alone”, and executed using accompanying scripts, with examples of
712 “map” (the northwest European Shelf simulation, as Fig. 3), “section” (Celtic
713 Sea) and “time series” (E1) simulations (`run_map`, `run_section` and
714 `run_timeseries`, respectively)
- 715 • /domain contains bathymetry and tide data for the northwest European Shelf
716 region (`s12_m2_s2_n2_h_map.asc`), for a selected north-south section in
717 the Celtic Sea (`s12_m2_s2_n2_h_sec.asc`) and for a selected point, E1
718 in the western English Channel (`s12_m2_s2_n2_h_tim.asc`)
- 719 • /met contains climatological meteorological forcing (`Celtic_met.dat`)
- 720 • /output contains example output data from the three runs (map, section,
721 time series)
- 722 • /plotting contains MATLAB scripts for plotting maps, sections and time
723 series (`plot_map`, `plot_section` and `plot_timeseries`,
724 respectively)

725 The ancillary files needed for simulations in the domains “Western English Channel”
726 and “East China and Yellow Seas”, and for a selection of years, are available on
727 request from the author (e-mail rm12@soton.ac.uk).

728

729 **Acknowledgments**

730 Jeff Blundell assisted with initial editing of the S2P3 source code. Ivan Haigh ran the
731 OSU Tidal Prediction Software to predict tidal current amplitudes in the East China
732 and Yellow Seas. Data at L4 and E1 were downloaded from
733 <http://www.westernchannelobservatory.org.uk/data> with thanks to the Western
734 Channel Observatory community. RM acknowledges the support of a 2013 Research
735 Bursary awarded by the Scottish Association for Marine Science. AH was partly
736 funded by a Natural Environment Research Council fellowship (NE/H015930/2). We
737 thank three anonymous reviewers for a series of insightful comments that helped us to
738 focus the paper.

739

740

741 **References**

742

743 Amante, C. and B. W. Eakins (2009). ETOPO1 1 Arc-Minute Global Relief Model:
744 Procedures, Data Sources and Analysis. NOAA Technical Memorandum
745 NESDIS NGDC-24, 19 pp.

746

747 Bauer, A., and J. J. Waniek (2013). Factors affecting the chlorophyll a concentration
748 in the central Beibu Gulf, South China Sea, *Mar. Ecol. Prog. Ser.*, **474**, 67-88,
749 doi:103354/meps10075

750

751 Edwards, K. P., Barciela, R., and M. Butenschön (2012). Validation of the NEMO-
752 ERSEM operational ecosystem model for the North West European Continental
753 Shelf, *Ocean Sci.*, **8**, 983-1000, doi:10.5194/os-8-983-2012.

754

755 Egbert, G. D., Bennett, A. F., and M. G. G. Foreman (1994). TOPEX/POSEIDON
756 tides estimated using a global inverse model. *J. Geophys. Res.*, **99**, 24821-
757 24852, doi:10.1029/94JC01894

758

759 Egbert, G. D., and S. Y. Erofeeva (2002). Efficient Inverse Modeling of Barotropic
760 Ocean Tides. *J. Atmos. Oceanic Technol.*, **19**, 183–204. doi:
761 [http://dx.doi.org/10.1175/1520-0426\(2002\)019<0183:EIMOBO>2.0.CO;2](http://dx.doi.org/10.1175/1520-0426(2002)019<0183:EIMOBO>2.0.CO;2)

762

763 Geider, R. J., MacIntyre, H. L., and T. M. Kana (1997). A dynamic model of
764 phytoplankton growth and acclimation: responses of the balanced growth rate
765 and chlorophyll a:carbon ratio to light, nutrient-limitation and
766 temperature. *Mar. Ecol. Prog. Ser.*, **148**, 187-200.

767

768 Gong, G.-C., Wen, Y.-H., Wang, B.-W., and G.-J. Liu (2003). Seasonal variation of
769 chlorophyll a concentration, primary production and environmental conditions
770 in the subtropical East China Sea. *Deep-Sea Research II*, **50**, 1219–1236,

771

772 Groom, S., Martinez-Vicente, V., Fishwick, J., Tilstone, G., Moore, G., Smyth, T.,
773 and D. Harbour (2009). The Western English Channel Observatory: optical
774 characteristics of station L4. *J. Mar. Sys.*, **77**, 278-295.

775

776 Hickman, A. E., Holligan, P. M., Moore, C. M., Sharples, J., Krivtsov, V. and M. R.
777 Palmer (2009). Distribution and chromatic adaptation of phytoplankton within a
778 shelf sea thermocline. *Limnol. Oceanogr.*, **54**, 525-536.

779

780 Hickman, A. E., Moore, C. M., Sharples, J., Lucas, M. I., Tilstone, G. H., Krivtsov, V.
781 and P. M. Holligan (2012). Primary production and nitrate uptake within the
782 seasonal thermocline of a stratified shelf sea. *Mar. Ecol. Prog. Ser.*, **463**, 39-57,
783 doi:10.3354/meps09836

784

785 Hickox R., I. Belkin, P. Cornillon and Z. Shan (2000). Climatology and Seasonal
786 Variability of Ocean Fronts in the East China, Yellow and Bohai Seas from
787 Satellite SST Data. *Geophys. Res. Lett.*, **27**, 2945-2948.

788

789 Hill, A. E., James, I. D., Linden, P. F., Matthews, J. P., Prandle, D., Simpson, J. H.,
790 Gmitrowicz, E. M., Smeed, D. A., Lwiza, K. M. M., Durazo, R., Fox, A. D., and
791 D. G. Bowers (1993). Dynamics of tidal mixing fronts in the North Sea [and
792 discussion]. *Phil. Trans. Roy. Soc. Lond. (A)*, **343**, 1669 (1993): 431-446.

793

794 Hill, A. E., J. Brown, L. Fernand, J. Holt, K. J. Horsburgh, R. Proctor, R. Raine, and
795 W. R. Turrell (2008). Thermohaline circulation of shallow tidal seas. *Geophys.*
796 *Res. Lett.*, **35**, L11605, doi:10.1029/2008GL033459.

797

798 Holligan P. M., Williams, P. J. L., Purdie, D., and R. P. Harris (1984) Photosynthesis,
799 respiration and nitrogen supply of plankton populations in stratified, frontal and
800 tidally mixed shelf waters. *Mar. Ecol. Prog. Ser.*, **17**, 201–213.

801

802 Holt, J., Harle, J., Proctor, R., Michel, S., Ashworth, M., Batstone, C., Allen, I.,
803 Holmes, R., Smyth, T., Haines, K., Bretherton, D., and G. Smith (2009).
804 Modelling the global coastal ocean. *Phil. Trans. Roy. Soc. A*, **367**, 939-951, doi:
805 10.1098/rsta.2008.0210

806

807 Holt, J., Wakelin, S., and J. Huthnance (2009). Down-welling circulation of the
808 northwest European continental shelf; A driving mechanism for the continental

809 shelf carbon pump. *Geophys. Res. Lett.*, **36**, L14602,
810 doi:10.1029/2009GL038997
811

812 Huthnance, J. M., Holt, J. T., and S. L. Wakelin (2009). Deep ocean exchange with
813 west-European shelf seas. *Ocean Sci.*, **5**, 621–634, www.ocean-
814 sci.net/5/621/2009/
815

816 Joint, I., and S. B. Groom (2000). Estimation of phytoplankton production from
817 space: current status and future potential of satellite remote sensing. *J. Exp.*
818 *Mar. Biol. Ecol.*, **250**, 233-255.
819

820 Kalnay, E., Kanamitsu, M., and R. Kistler (1996). The NCEP/NCAR 40-year
821 reanalysis project, *Bull. Amer. Meteor. Soc.*, **77**, 437-470.
822

823 Moore, C. M., Suggett, D. J., Hickman, A. E., Kim, Y. N., Tweddle, J. F., Sharples,
824 J., Geider, R. J. and P. M. Holligan (2006). Phytoplankton photoacclimation and
825 photoadaptation in response to environmental gradients in a shelf sea. *Limnol.*
826 *Oceanogr.*, **51**, 936-949.
827

828 Moore, C. M., Suggett, D., Holligan, P. M., Sharples, J., Abraham, E. R., Lucas, M.
829 I., Rippeth, T. P., Fisher, N. R., Simpson, J. H., and D. J. Hydes (2003).
830 Physical controls on phytoplankton physiology and production at a shelf sea
831 front: a fast repetition-rate fluorometer based field study *Mar. Ecol. Prog. Ser.*,
832 **259**, 29–45.
833

834 O'Dea, E. J., Arnold, A. K., Edwards, K. P., Furner, R., Hyder, P., Martin, M. J.,
835 Siddom, J. R., Storkey, D., While, J., Holt, J. T., and H. Liu (2012). An
836 operational ocean forecast system incorporating NEMO and SST data
837 assimilation for the tidally driven European North-West shelf. *Journal of*
838 *Operational Oceanography*, **5** (1). 3-17.
839

840 Pemberton, K., Rees, A. P., Miller, P. I., Raine, R., and I. Joint (2004). The influence
841 of water body characteristics on phytoplankton diversity and production in the
842 Celtic Sea. *Cont. Shelf Res.*, **24**, 2011–2028.

843

844 Pingree, R., Holligan, P., and G. T. Mardell (1978). The effects of vertical stability on
845 phytoplankton distributions in the summer on the northwest European Shelf.
846 *Deep Sea Res.*, **25**, 1011–1028.

847

848 Rees, A. P., Joint, I., and K. M. Donald (1999). Early spring bloom phytoplankton-
849 nutrient dynamics at the Celtic Sea Shelf Edge. *Deep Sea Research II*, **46**, 483–
850 510.

851

852 Sharples, J., (1999). Investigating the seasonal vertical structure of phytoplankton in
853 shelf seas. *Marine Models Online*. **1**, 3-38.

854

855 Sharples, J., Ross O.N., Scott, B.E., Greenstreet, S., Fraser, H. (2006). Inter-annual
856 variability in the timing of stratification and the spring bloom in the North-
857 western North Sea. *Cont. Shelf Res.*, **26**, 733-751.

858

859 Sharples, J., Tweddle, J. F., Green, J. A. M., Palmer, M. R., Kim, Y.-N., Hickman, A.
860 E., Holligan, P. M., Moore, C. M., Rippeth, T. P., Simpson, J. H., and V.
861 Krivtsov (2007). Spring-neap modulation of internal tide mixing and vertical
862 nitrate fluxes at a shelf edge in summer. *Limnol. Oceanogr.*, **52**, 1735-1747.

863

864 Sharples, J. (2008). Potential impacts of the spring-neap tidal cycle on shelf sea
865 primary production. *Journal of Plankton Research*, **30**, 183-197.

866

867 Simpson, J. H., and J. R. Hunter (1974). Fronts in the Irish Sea. *Nature*, **250**, 404-406.

868

869 Simpson, J. H., and D. G. Bowers (1984). Geographical variations in the seasonal
870 heating cycle in northwest European shelf seas. *Annales Geophysicae*, **2**(4),
871 411-416.

872

873 Simpson, J. H., and J. Sharples (2012). *Introduction to the Physical and Biological*
874 *Oceanography of Shelf Seas*. Cambridge University Press.

875

876 Smyth, T. J., Fishwick, J. R., Al-Moosawi, L., Cummings, D. G., Harris, C., Kitidis,

877 V., Rees, A., Martinez-Vicente, V., and E. M. S. Woodward (2010). A broad
878 spatio-temporal view of the Western English Channel observatory. *J. Plankton*
879 *Res.*, **32**, 585-601. doi: 10.1093/plankt/fbp128
880
881 Son, S., Yoo, S., and J.-H. Noh (2006). Spring phytoplankton bloom in the fronts of
882 the East China Sea. *Ocean Sci. J.*, **41**, 181-189. doi:10.1007/BF03022423
883
884 Weston, K., Fernand, L., Mills, D., Delahunty, R., and J. Brown (2005). Primary
885 production in the deep chlorophyll maximum of the central North Sea. *J*
886 *Plankton Res.*, **27**, 909–922.
887
888 Zhu, J., Hu, J., and Z. Liu (2013). On summer stratification and tidal mixing in the
889 Taiwan Strait, *Frontiers of Earth Science*, **7**, 141-150, doi:10.1007/s11707-013-
890 0355-1.

891 **Figure Captions**

892

893 Figure 1. Bottom depth (relative to sea surface) in the three S2P3-R domains: (a)
894 northwest European shelf; (b) western English Channel; (c) East China and Yellow
895 Seas.

896

897 Figure 2. Daily meteorological data: climatological for the northwest European shelf
898 (Sharples, 2008), and for 2013 in the Western English Channel, and in the East China
899 and Yellow Seas: (a) air temperature; (b) wind speed; (c) cloud fraction; (d) relative
900 humidity.

901

902 Figure 3. For the northwest European shelf domain: (a) Hunter-Simpson parameter,
903 highlighting the contour delineating $\log_{10}(h/u^3) = 2.7$; (b) day 190 surface-bottom
904 temperature difference; (c) net surface heat flux; (d) annual net production. In (a), we
905 label fronts as in Fig. 8.1 of Simpson and Sharples (2012): the Islay front (A); the
906 Western Irish Sea front (B); the Cardigan Bay front (C); the St. Georges Channel
907 front (D); the Ushant and Western English Channel front (E). We additionally label
908 the Flamborough frontal system (F).

909

910 Figure 4. Sections through the Celtic Sea front around day 215 of 2003: (a) locations
911 of CTD stations (dots) and model grid-points (circles); (b), (c) observed and modelled
912 temperature ($^{\circ}\text{C}$); (d), (e) observed and modeled dissolved inorganic nitrate (units
913 mmol m^{-3}); (f), (g) observed and modelled chl-a concentration (units mg chl-a m^{-3}).
914 The locations of observations in profile are indicated by dots in (b), (d) and (f).

915

916 Figure 5. Surface–bottom temperature differences ($^{\circ}\text{C}$) in the Western English
917 Channel, on day 190 of 2002-13. Coloured circles indicate the coincident temperature
918 differences at L4 and E1, subject to data availability (E1 data are unavailable in 2004,
919 2006 and 2013).

920

921 Figure 6. Time series of surface-bottom temperature differences observed and (daily)
922 simulated at L4 and E1 (<http://www.westernchannelobservatory.org.uk/data.php>).

923

924 Figure 7. Sections through the developing tidal mixing front east of Lizard peninsula,
925 along 50.017°N, on days 100, 130, 160 and 190 of 2013: temperature (left column);
926 dissolved inorganic nitrate (mmol m^{-3} , middle column); chl-a (mg chl-a m^{-3} , right
927 column).

928

929 Figure 8. Time series of surface and bottom temperature (red and blue curves),
930 surface-bottom temperature difference, surface DIN and surface chl-a concentrations,
931 across the tidal mixing front east of the Lizard peninsula in 2013.

932

933 Figure 9. For the East China and Yellow Seas domain in 2013: (a) Hunter-Simpson
934 parameter, highlighting the contour delineating $\log_{10}(h/u^3) = 2.7$; (b) day 190 surface-
935 bottom temperature difference; (c) net surface heat flux; (d) annual net production.

936

937 Figure 10. Sections through the developing tidal mixing front of the East China Sea,
938 along 32°N, on days 100, 130, 160 and 190 of 2013: temperature (left column); DIN
939 (mmol m^{-3} , middle column); chl-a (mg chl-a m^{-3} , right column).

940

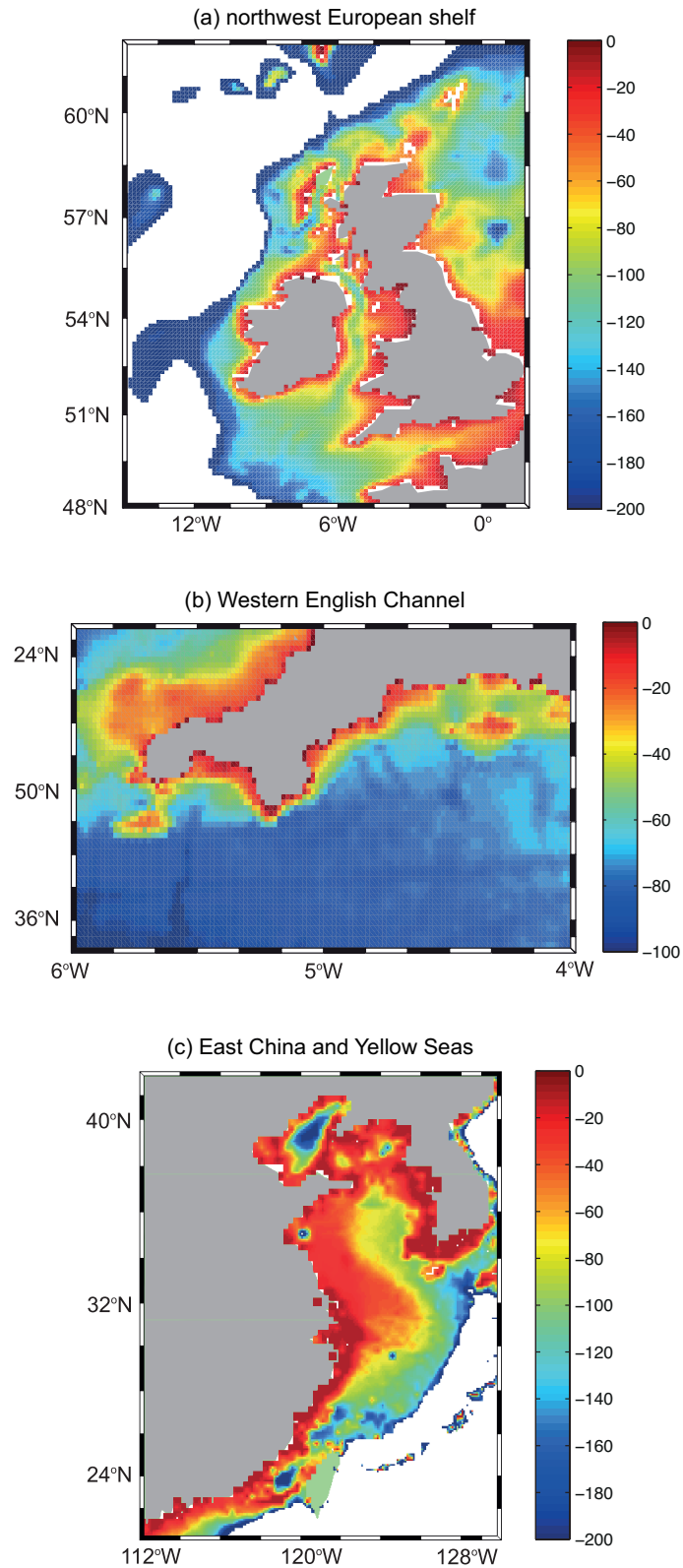
941 Figure 11. Surface-bottom temperature differences ($^{\circ}\text{C}$) across the southern Celtic Sea
942 and western English Channel, in mid July of 2014, simulated with S2P3-R configured
943 in twelve $1^{\circ} \times 1^{\circ}$ sub-domains, as indicated.

944 Table 1. Boundaries, resolution, tidal forcing, initial temperature and meteorological
 945 forcing for each domain (POLCOMS = Proudman Oceanographic Laboratory Coastal
 946 Ocean Modelling System; OTPS = OSU Tidal Prediction Software)

947

Domain	Boundaries	Resolution	Tidal Forcing	Initial temperature field	Meteorological forcing
northwest European shelf	14.917°W – 1.917°E 48.056°N – 61.944°N	0.167° (longitude) 0.111° (latitude) (~12 km)	M2, S2, N2 (POLCOMS)	10.1°C everywhere (default)	Daily climatology for the Celtic Sea (Sharples, 2008)
Western English Channel	4 – 6°W 49.5 – 50.5°N	1' x 1' (~1 km)	M2, S2, N2 (POLCOMS interpolated)	10.1°C everywhere	Daily NCEP reanalysis data for grid square centred on 5°W, 50°N
East China and Yellow Seas	112 – 130°E 21 – 42°N	0.083° x 0.083° (~6 km)	M2, S2, N2, O1, K1 (OTPS)	After 1-year started from 15.1°C everywhere	Daily NCEP reanalysis data for grid square centred on 125°E, 32.5°N

948



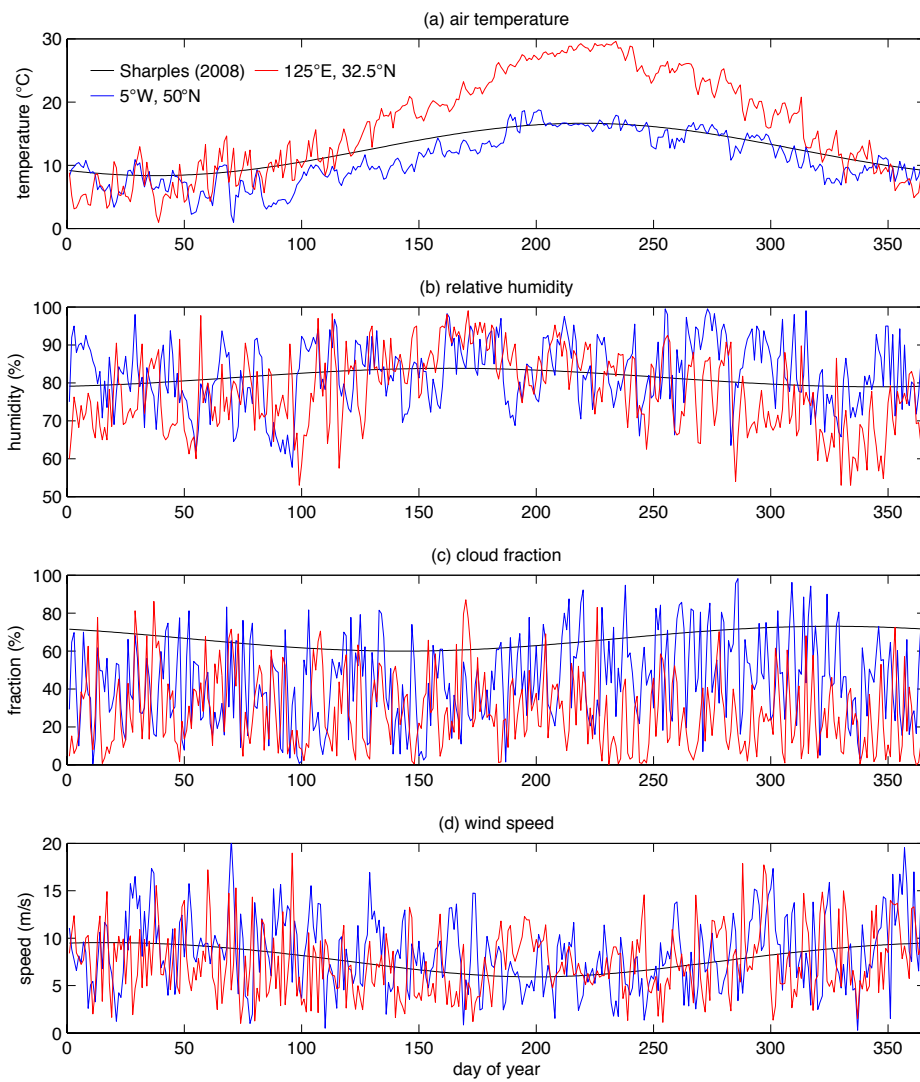
949

950

951 Figure 1. Bottom depth (relative to sea surface) in the three S2P3-R domains: (a)

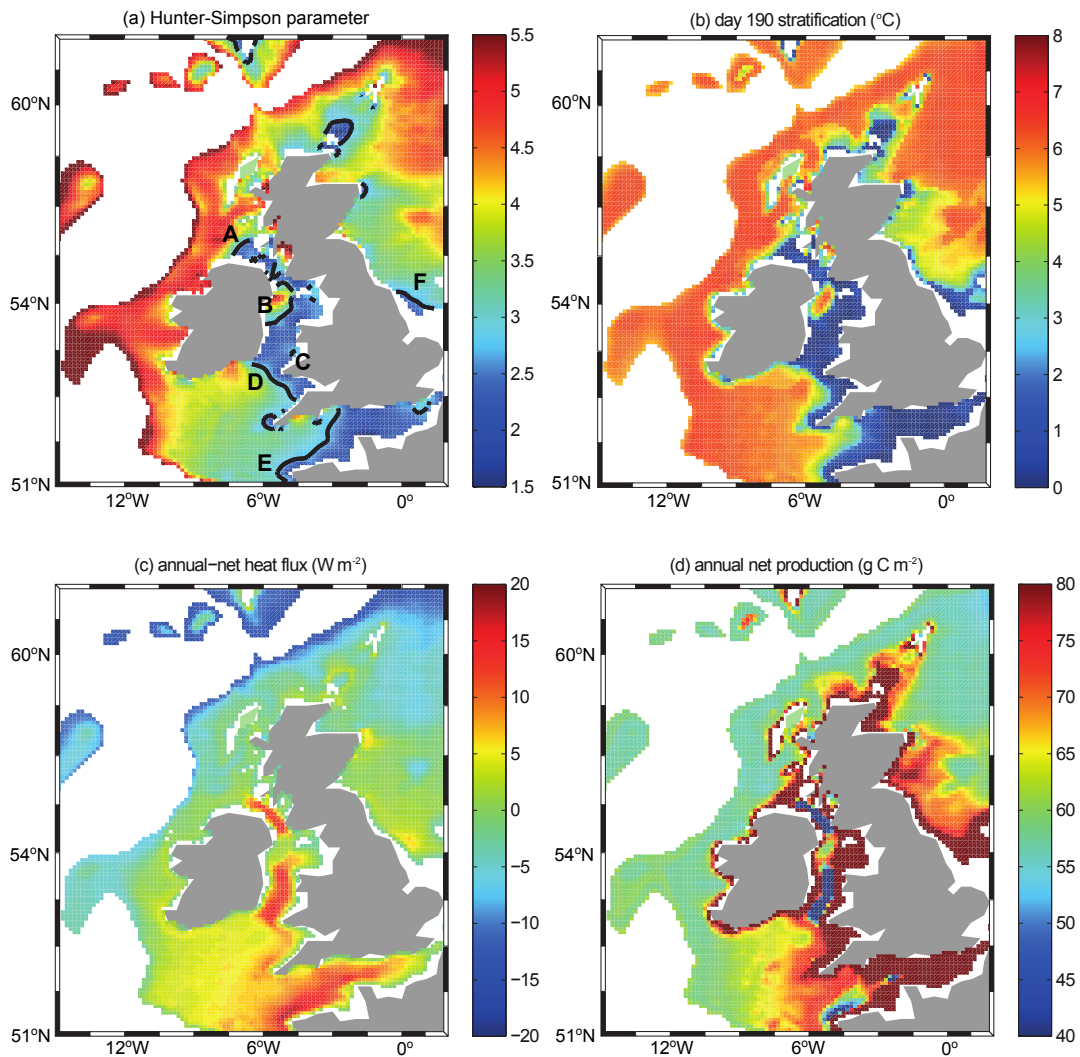
952 northwest European shelf; (b) western English Channel; (c) East China and Yellow

953 Seas.



954

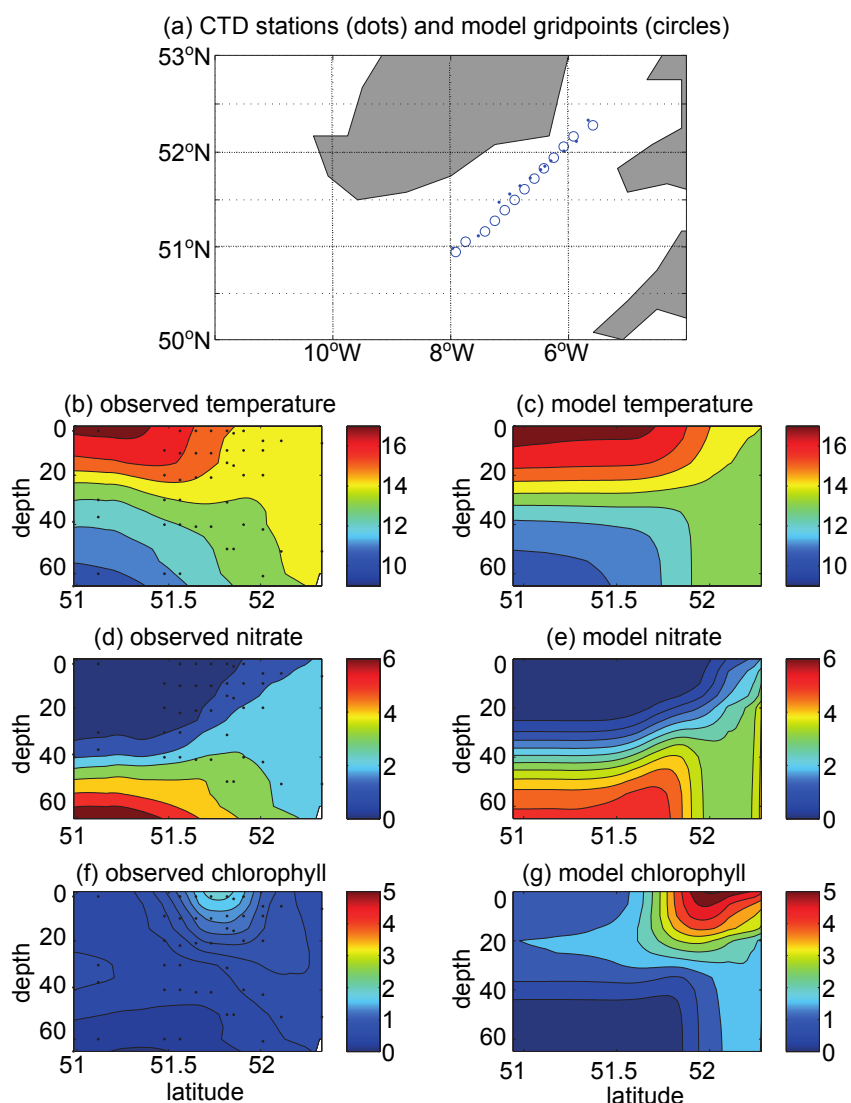
955 Figure 2. Daily meteorological data: climatological for the northwest European shelf
 956 (Sharples, 2008), and for 2013 in the Western English Channel, and in the East China
 957 and Yellow Seas: (a) air temperature; (b) wind speed; (c) cloud fraction; (d) relative
 958 humidity.



960

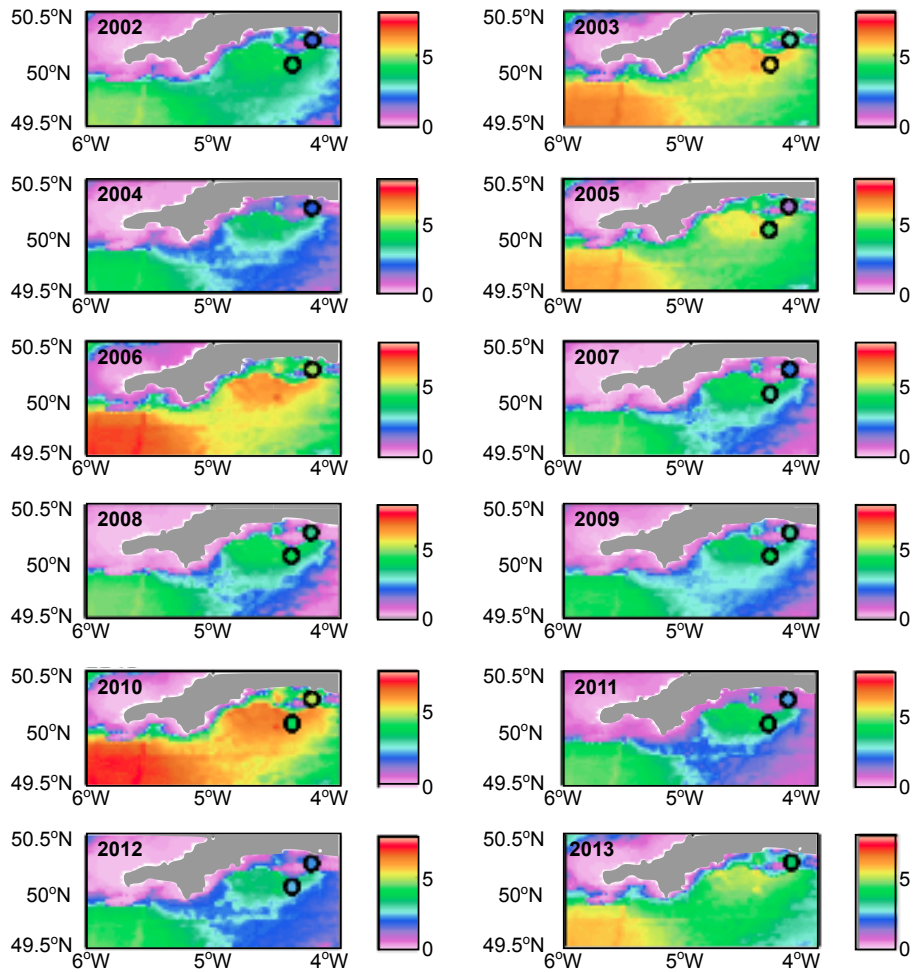
961

962 Figure 3. For the northwest European shelf domain: (a) Hunter-Simpson parameter,
 963 highlighting the contour delineating $\log_{10}(h/u^3) = 2.7$; (b) day 190 surface-bottom
 964 temperature difference; (c) net surface heat flux; (d) annual net production. In (a), we
 965 label fronts as in Fig. 8.1 of Simpson and Sharples (2012): the Islay front (A); the
 966 Western Irish Sea front (B); the Cardigan Bay front (C); the St. Georges Channel
 967 front (D); the Ushant and Western English Channel front (E). We additionally label
 968 the Flamborough frontal system (F).



969

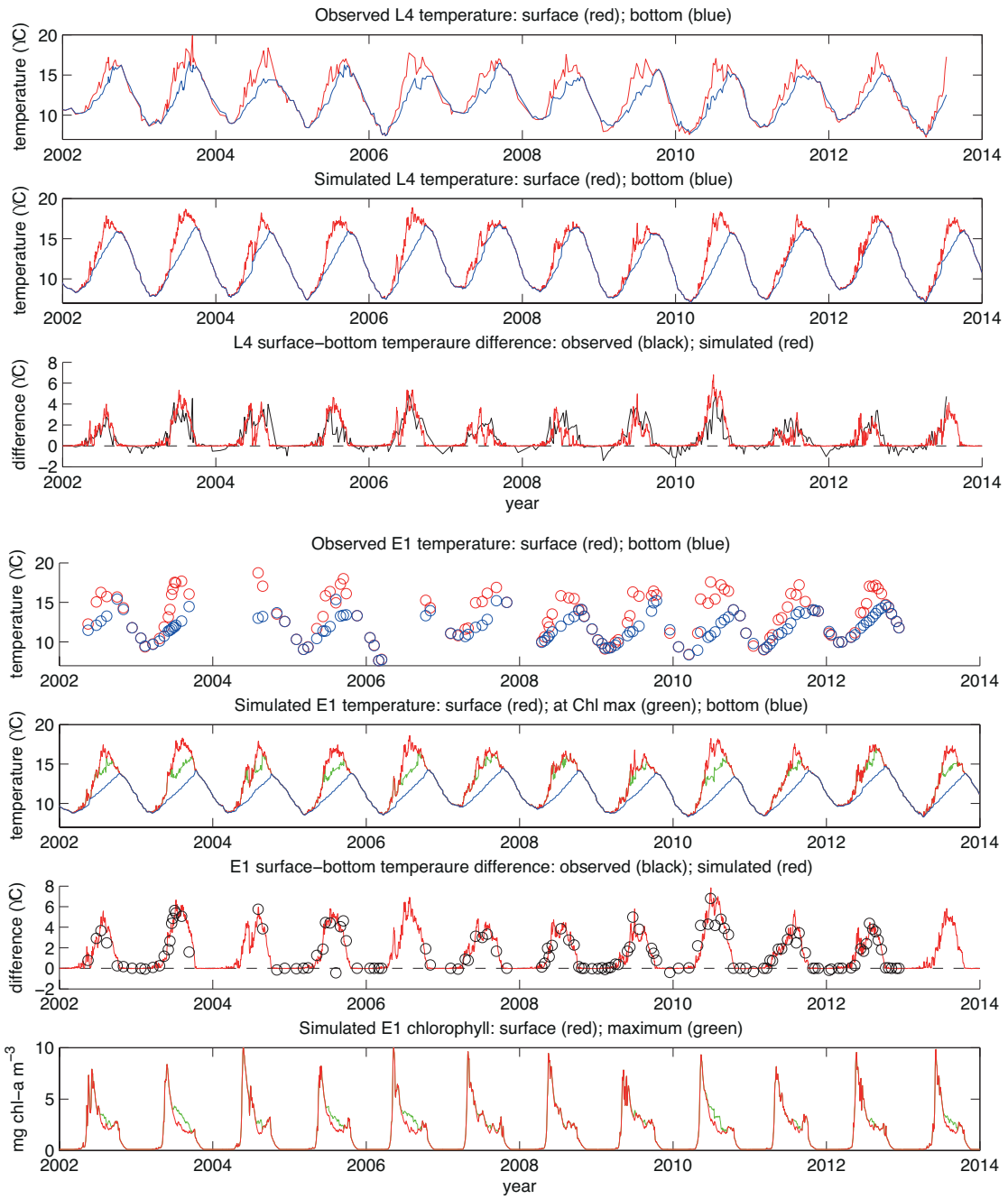
970 Figure 4. Sections through the Celtic Sea front around day 215 of 2003: (a) locations
 971 of CTD stations (dots) and model grid-points (circles); (b), (c) observed and modelled
 972 temperature ($^{\circ}\text{C}$); (d), (e) observed and modeled dissolved inorganic nitrate (units
 973 mmol m^{-3}); (f), (g) observed and modelled chl-a concentration (units mg chl-a m^{-3}).
 974 The locations of observations in profile are indicated by dots in (b), (d) and (f).



975

976

977 Figure 5. Surface–bottom temperature differences (°C) in the Western English
 978 Channel, on day 190 of 2002-13. Coloured circles indicate the coincident temperature
 979 differences at L4 and E1, subject to data availability (E1 data are unavailable in 2004,
 980 2006 and 2013).

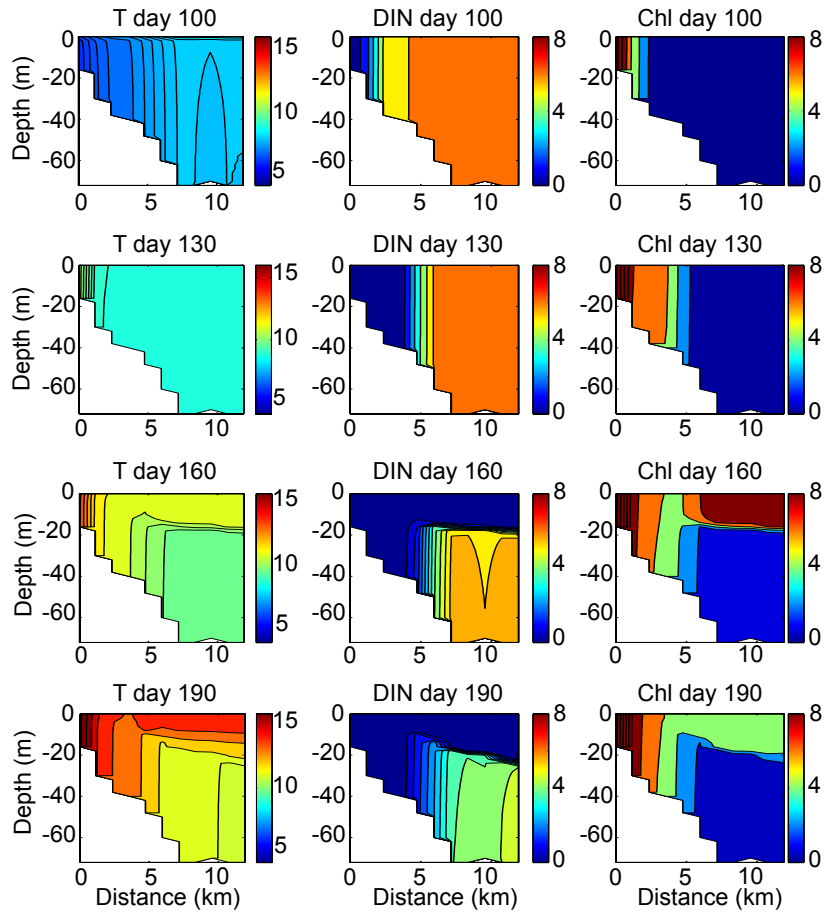


981

982

983 Figure 6. Time series of surface-bottom temperature differences observed and (daily)

984 simulated at L4 and E1 (<http://www.westernchannelobservatory.org.uk/data.php>).



985

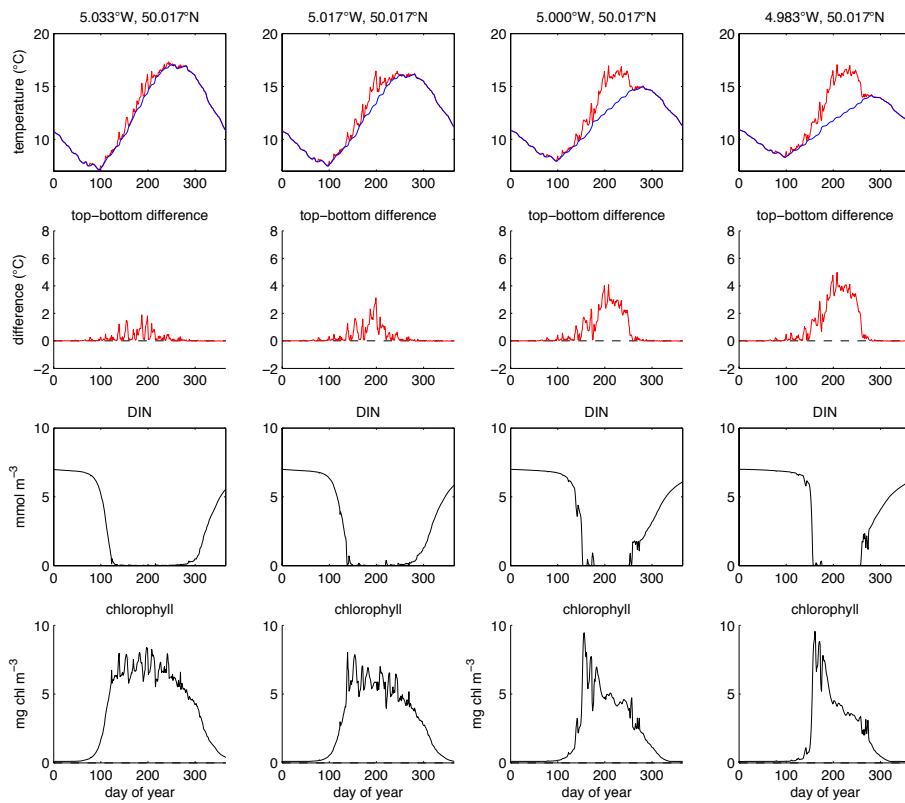
986

987 Figure 7. Sections through the developing tidal mixing front east of Lizard peninsula,

988 along 50.017°N, on days 100, 130, 160 and 190 of 2013: temperature (left column);

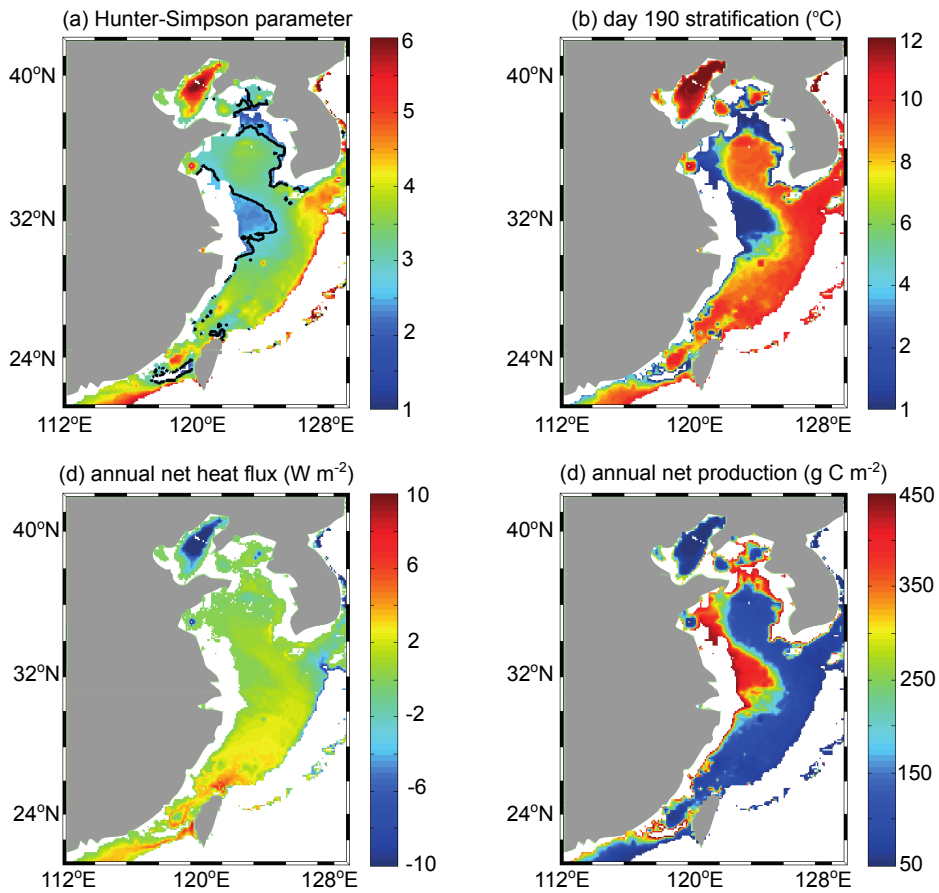
989 dissolved inorganic nitrate (mmol m^{-3} , middle column); chl-a (mg chl-a m^{-3} , right

990 column).



991

992 Figure 8. Time series of surface and bottom temperature (red and blue curves),
 993 surface-bottom temperature difference, surface DIN and surface chl-a concentrations,
 994 across the tidal mixing front east of the Lizard peninsula in 2013.

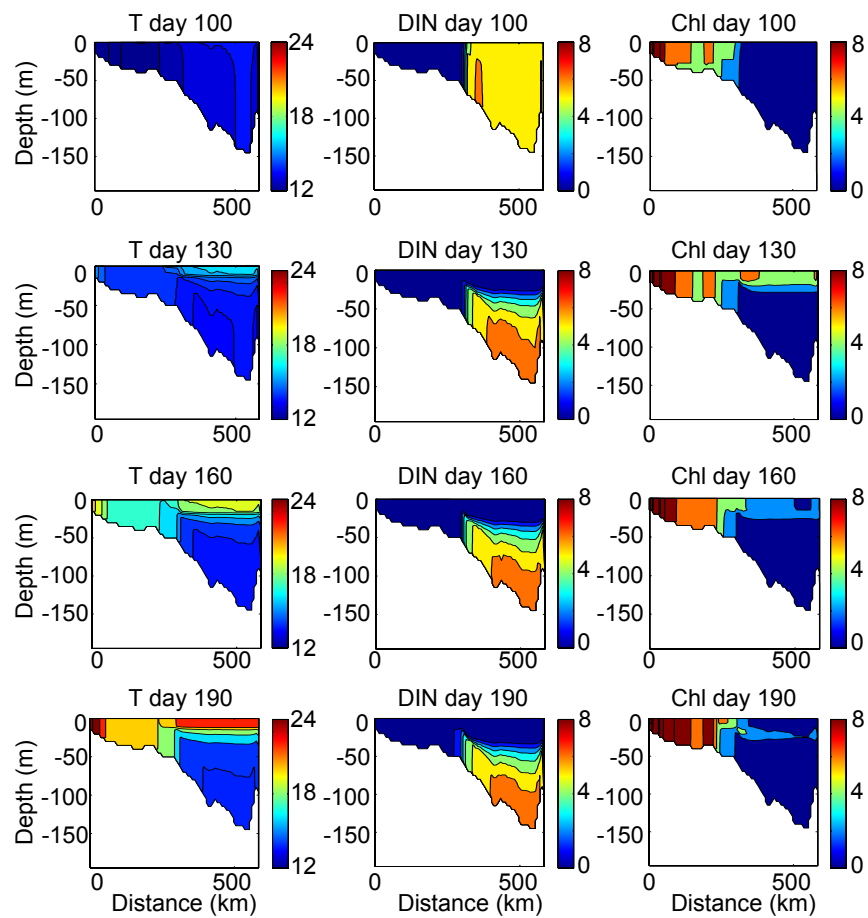


995

996

997 Figure 9. For the East China and Yellow Seas domain in 2013: (a) Hunter-Simpson
 998 parameter, highlighting the contour delineating $\log_{10}(h/u^3) = 2.7$; (b) day 190 surface-
 999 bottom temperature difference; (c) net surface heat flux; (d) annual net production.

1000



1001

1002

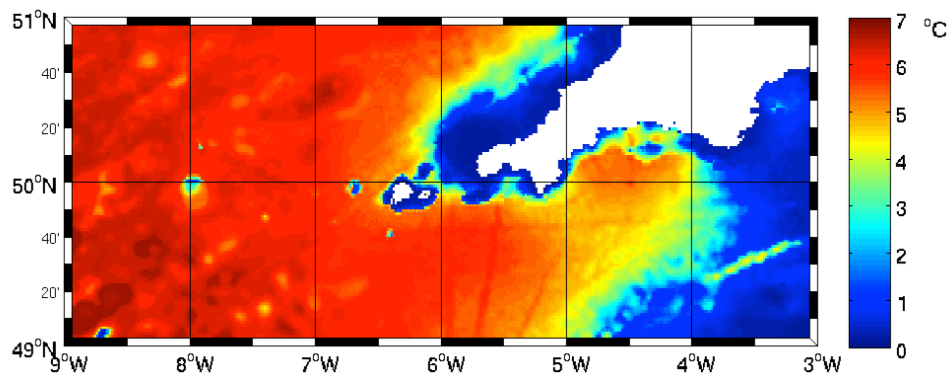
1003 Figure 10. Sections through the developing tidal mixing front of the East China Sea,

1004 along 32°N, on days 100, 130, 160 and 190 of 2013: temperature (left column); DIN

1005 (mmol m^{-3} , middle column); chl-a (mg chl-a m^{-3} , right column).

1006

1007



1008

1009 Figure 11. Surface-bottom temperature differences (°C) across the southern Celtic Sea
1010 and western English Channel, in mid July of 2014, simulated with S2P3-R configured
1011 in twelve 1° x 1° sub-domains, as indicated.